Sea level and circulation variability of the Gulf of Carpentaria: Influence of the Madden-Julian Oscillation and the adjacent deep ocean

E. C. J. Oliver[1] and K. R. Thompson[1]

[1] The Madden-Julian Oscillation (MJO) is a significant contributing factor to intraseasonal variability in both the tropical and extratropical atmosphere and ocean. Sea level and circulation variations in the Gulf of Carpentaria (northern Australia) and the coastal regions of the northeastern Indian Ocean and eastern Pacific have been shown to be related to the MJO. A nonlinear barotropic numerical model, validated with local tide gauge data, is used to study the Gulf of Carpentaria from 1979 to 2009. It is shown that the model reproduces well the seasonal cycle of sea level as well as intraseasonal variations and their seasonal modulations. Intraseasonal variability is shown to be driven by surface wind stress that is closely related to the MJO. The model is next used to remove the local wind effect from the tide gauge data, resulting in a low-frequency residual signal. This low-frequency signal is interpreted in terms of larger-scale modes of variability of the adjacent shelf seas and the Indian and Pacific oceans through comparison with climatological indices, correlations with regional sea level measured by altimeters, and Hovmöller diagrams. It is shown that this signal is generated in the Pacific and related to the El Niño–Southern Oscillation. The implications for predictability and forecasting in the Gulf of Carpentaria on intraseasonal timescales are discussed.

1. Introduction

[2] Over recent decades there has been an increased interest in understanding and characterizing intraseasonal variability in the world's oceans and global atmosphere. Variability on these timescales bridges the gap between weather, which occurs on timescales less than about 2 weeks, and climate, which occurs on much longer timescales. Earlier studies were restricted by primitive numerical models, low computing power, and limited observational coverage of the globe. Over recent decades, much improved models, as well as a better understanding of the intraseasonal dynamics of the ocean and atmosphere, have paved the way for a number of realistic studies of intraseasonal variability in the ocean-atmosphere system.

[3] The dominant mode of intraseasonal variability in the tropical atmosphere is the Madden-Julian Oscillation [*Madden and Julian*, 1971, 1972]. The Madden-Julian Oscillation (MJO) is a quasi-periodic phenomenon that originates over the tropical Indian Ocean as a region of anomalous deep convection and precipitation. It is observed as variations in tropical outgoing longwave radiation and zonal wind on timescales between 30 and 90 days with a peak in energy around 40–50 days [e.g., *Zhang*, 2005]. This initial condition in the tropical Indian Ocean then propagates eastward along the equator, losing much of its strength after it leaves the warm waters of the western Pacific, and finally dissipates over the Atlantic Ocean and Africa. The MJO features a prominent seasonal cycle in its mean position and strength.

[4] Although originating in the tropical atmosphere, the MJO can affect the extratropics as well as the oceans. It has been demonstrated that the MJO can be related to the rate of tropical cyclone generation in all three ocean basins [*Liebmann et al.*, 1994; *Maloney and Hartmann*, 2000a, 2000b; *Hall et al.*, 2001], rainfall variability in the U.S. Pacific Northwest [*Bond and Vecchi*, 2003], high-latitude surface air temperatures [*Vecchi and Bond*, 2004; *Lin and Brunet*, 2009], and the North Atlantic Oscillation [*Cassou*, 2008; *Lin et al.*, 2009]. Connections have also been found with sea surface temperature [*Shinoda et al.*, 1998; *Maloney et al.*, 2008] and sea level [*Fu*, 2003]. The work of *Oliver and Thompson* [2010], hereafter referred to as OT10, found that sea level from many ocean regions, including the equatorial Pacific, the west coast of the American continent, the Gulf of Carpentaria, and the northeastern Indian Ocean, have significant correlations with the MJO. Building on the earlier work of *Spillane et al.* [1987] and *Enfield* [1987], they found that waves traveling across the equatorial Pacific,

---

[1]Department of Oceanography, Dalhousie University, Halifax, Nova Scotia, Canada.
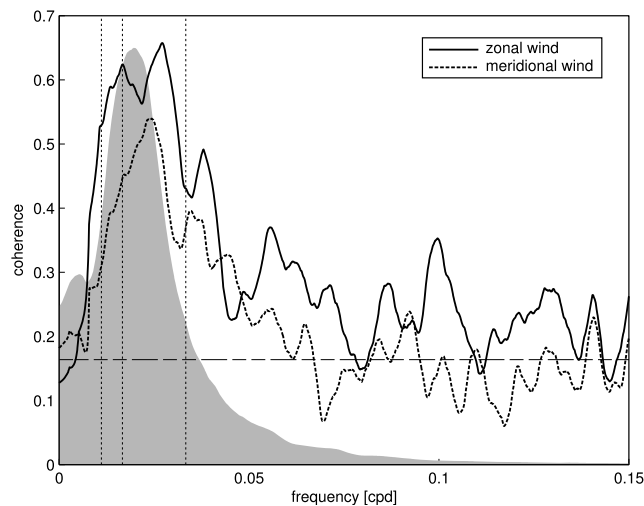
Figure 1. Power spectrum of the MJO and its relationship to wind over the Gulf of Carpentaria. The two lines show the coherence between the MJO and zonal (solid) and meridional (dashed) surface wind averaged over the box shown in Figure 3. The horizontal dashed line indicates the 5% significance level and vertical lines indicate periods of 30, 60, and 90 days. The shaded region shows the shape of the power spectrum of the MJO index. (The spectra of the two individual components have been summed.)

generated by MJO-related surface winds [e.g., *Zhang et al.*, 2009], excite coastally trapped waves along the Americas that are detected poleward as far as 37°N and 33°S. They also showed that the MJO is related to a complex mode of variability in the northeastern Indian Ocean in which eastward traveling equatorially trapped waves generated by surface winds can excite coastally trapped waves along the Sumatran coast followed by Rossby waves which are then reflected back into the interior of the basin. This phenomenon was also observed by *Vialard et al.* [2009] and *Webber et al.* [2010].

[5] In this study we examine the effect of the Madden-Julian Oscillation on sea level in the Gulf of Carpentaria in more detail than in OT10, and we expand the analysis to include circulation variability. This is done using a regional ocean model that is validated through comparison with coastal tide gauge observations. The dynamics on intraseasonal timescales is shown to be simple wind-driven setup of sea level. The wind forcing, and thus the sea level and circulation, are also shown to be strongly related to the MJO. The sea level response exhibits a strong seasonality which is related to both the timing of the Australian monsoon and the seasonal structure of the Madden-Julian Oscillation itself. By removing that component of sea level related to local wind, a low-frequency residual variation of sea level in the gulf is obtained. We show, through a variety of statistical techniques, that the Pacific Ocean is the source of this low-frequency variability in the Gulf of Carpentaria.

[6] From a scientific perspective we are interested in exploring the coastal expressions of the Madden-Julian Oscillation as well as lower frequency variability such as the El Niño–Southern Oscillation (ENSO) in the Gulf of Carpentaria. From a more applied perspective we note that the gulf is an important fishing area and understanding how

environmental changes can affect these fisheries is potentially important from a resource management perspective. It has already been shown that ENSO affects rock lobster populations off the northwest coast of Australia through changes in sea level and circulation [*Pearce and Phillips*, 1988] and wind variability has been shown to affect the banana prawn fishery in the northern Gulf of Carpentaria [*Vance et al.*, 1985].

[7] This paper is organized as follows. The observations and a preliminary statistical analysis are presented in sections 2 and 3, respectively. The model is described in section 4, and in section 5 it is used to better understand the dynamics in the Gulf of Carpentaria and the role of the Madden-Julian Oscillation. In section 6, the low-frequency residual signal (i.e., that component not predicted by the model) is related to remote forcing from the Pacific and Indian oceans via the Indonesian Throughflow region. A summary of the results and implications of this study as well as a discussion of future work are presented in section 7.

2. Observations of Sea Level, the MJO, and Surface Wind

[8] We present here observations of the MJO, sea level, and the wind data which are used to validate and force the coastal model as a prelude to the more complete modeling study described in section 4. We supplemented the altimeter-based observations of sea level, which were used in OT10, with coastal observations from tide gauges.

### 2.1. The Madden-Julian Oscillation Index

[9] The MJO is characterized using the bivariate index of *Wheeler and Hendon* [2004]. Daily values from 1 January 1979 to 30 January 2010 were obtained from the Government of Australia Bureau of Meteorology (see http://www. bom.gov.au/bmrc/clfor/cfstaff/matw/maproom/RMM/index. htm). This index is based on the first two principal components calculated from observed tropical outgoing longwave radiation and zonal winds (after removing seasonal and interannual signals). These two time series describe an oscillating phenomenon with periods between 30 and 90 days and are approximately in quadrature. See the shaded region in Figure 1 for the power spectrum of the index.

2.2. Sea Level From Altimeters

[10] Global fields of altimeter measurements of sea level anomalies were obtained from Aviso (see http://www.aviso. oceanobs.com/en/home/index.html). The data were isostatically adjusted for local pressure effects and corrected for tides by Aviso. We analyzed weekly data from a 1/4° resolution grid for the period 14 October 1992 to 22 July 2009. The annual cycle and its first two harmonics were removed from each grid point time series using least squares prior to analysis.

2.3. Sea Level From Tide Gauges

[11] Hourly time series of sea level were obtained from three tide gauge locations (Figure 3) around the Gulf of Carpentaria for the period 14 November 1979 to 30 January 2010. The data for Groote Eylandt were obtained from the Australian Baseline Sea Level Monitoring Project (see
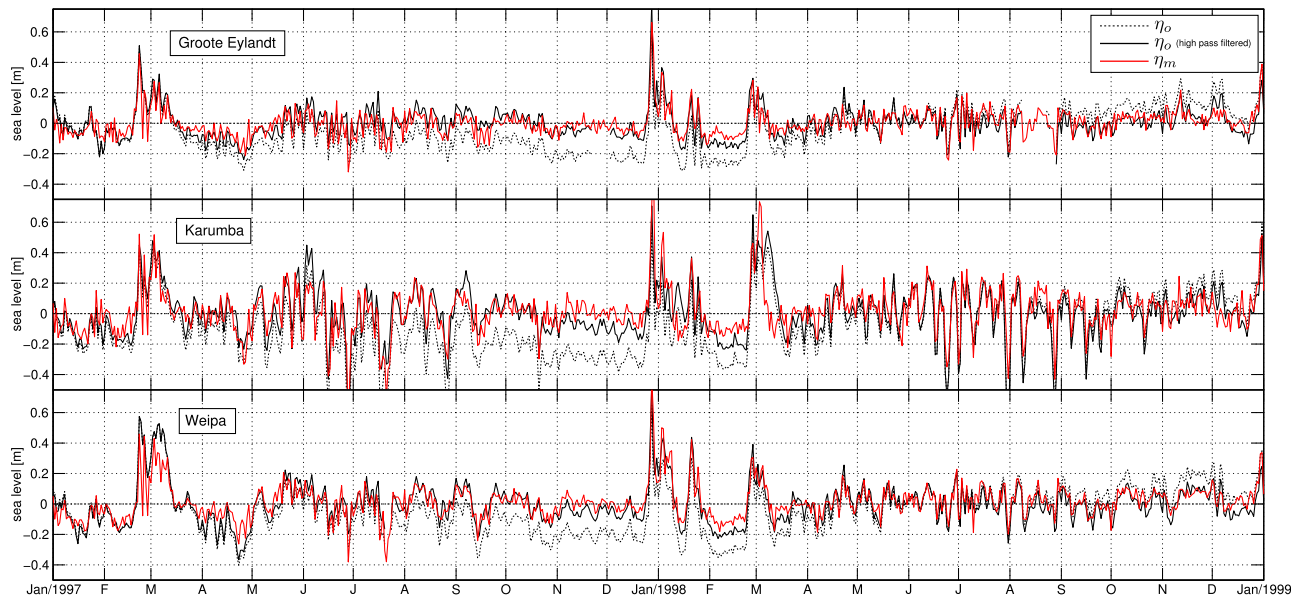
Figure 2. Observed and predicted sea level for a typical 2 year period. The dashed line shows the observed sea level (η_o) and the red line shows the corresponding model prediction (η_m). The solid line shows the observed sea level after high-pass filtering with a cutoff period of half a year.

http://www.bom.gov.au/oceanography/projects/abslmp/data/index.shtml) and those for Karumba and Weipa were obtained from Maritime Safety Queensland, Queensland Government, Australia. See Table 1 for details. The records were de-tided using the analysis package of *Pawlowicz et al.* [2002] using 66 tidal constituents and averaged to daily values using a simple Doodson X0 filter [*Doodson*, 1928]. The inverse barometer effect was removed using daily sea level pressures from the National Centers for Environmental Prediction (NCEP)/National Center for Atmospheric Research Reanalysis 1 [*Kalnay et al.*, 1996] defined on a 2.5° grid. The annual cycle and its first two harmonics were removed using least squares prior to analysis. The daily mean tidal residual of coastal sea level is denoted by η_o. Sample plots of the time series are shown in Figure 2.

2.4. Surface Wind

[12] Six-hourly fields of surface (10 m) winds were obtained from the NCEP/Department of Energy (DOE) Reanalysis 2 [*Kanamitsu et al.*, 2002] for the period 1 January 1979 to 31 December 2009. The data are defined on a global T62 Gaussian grid with an approximate resolution of 2°. The wind fields were mapped onto the ocean model grid (see section 4) using two-dimensional bicubic inter-

polation and stresses were subsequently calculated using the air-sea drag coefficient of *Large and Pond* [1981]. This drag formula ignores the stability of the atmosphere lying over the ocean surface. This is not a major concern because *McBride and Frank* [1999] have shown that the atmospheric stratification over the Gulf of Carpentaria is weak. We define the gulf mean wind as the average over the area shown by the box in Figure 3 (data over land and ocean are included).

3. Intraseasonal Variability in Observed Sea Level and Surface Wind

[13] The annual cycle of η_o was estimated for each tide gauge location by harmonic regression. Phases are similar across all stations, with sea level peaking in late January and February, and amplitudes are between 20 and 40 cm, consistent with the work of *Forbes and Church* [1983]. OT10 showed that a significant part of the intraseasonal variability of sea level in the Gulf of Carpentaria can be related the MJO. The MJO was found to account for up to 60% of the standard deviation of sea level in the gulf (after filtering out seasonal and interannual variability). They speculated that the underlying principal cause of this statistical relationship

Table 1. Details on the Tide Gauge Records[a]

Tide Gauge	Latitude (S)	Longitude (E)	Start Date	End Date	Complete (%)
Groote Eylandt	13° 50′	136° 30′	1 Sep 1993	31 Aug 2009	99
Karumba 1	17° 29′	140° 49′	14 Nov 1979	13 Mar 1991	96
Karumba 2	17° 29″	140° 49′	13 Oct 1993	30 Jan 2010	98
Weipa 1	12° 40′	141° 52′	1 Jun 1984	4 Sep 1991	95
Weipa 2	12° 40′	141° 52′	5 Sep 1991	1 Jan 2010	99

[a]The Karumba and Weipa records were split into two segments because there was a large gap in the middle of the record that was too long to fill by standard interpolation.
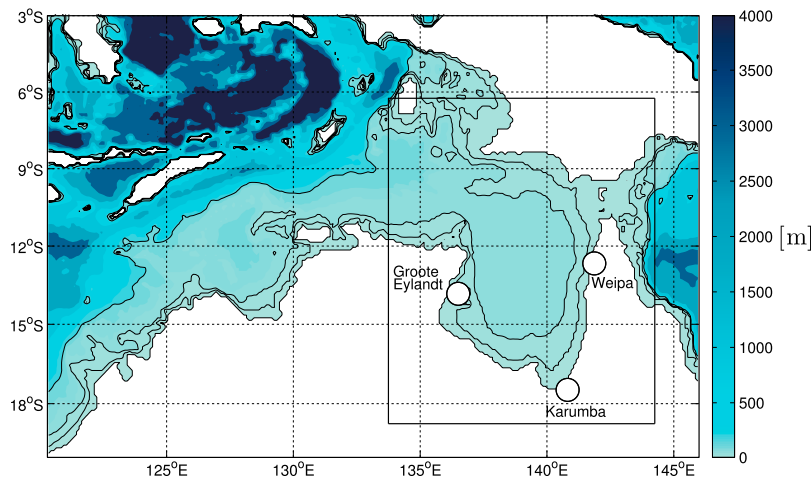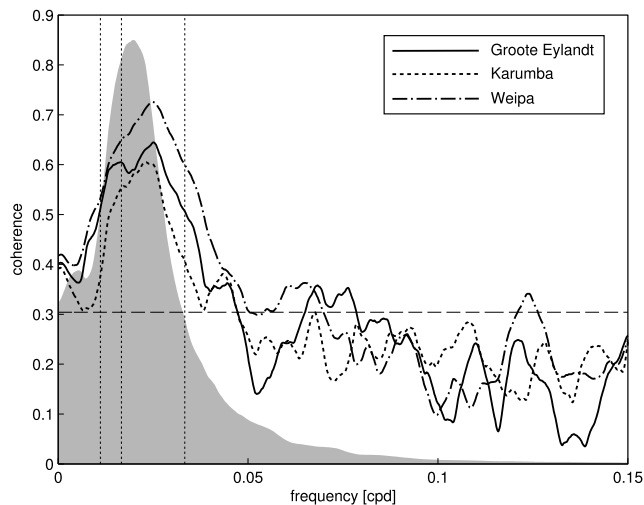
Figure 3. The model domain and bathymetry. Black lines show the 25, 50, and 200 m depth contours. The three white circles show the locations of the tide gauges. The box shows the area used to form the gulf mean wind and sea level (see sections 3 and 5).

was set up by local surface winds that are strongly linked to the MJO. *Tregoning et al.* [2008] also examined the effect of wind on sea level setup in the Gulf of Carpentaria but did not relate the wind forcing to the MJO. Furthermore, the coherence between the MJO and η_o is statistically significant across the MJO band (see Figure 4).

[14] As a note on statistical methods, we use the conventional definition of coherence [e.g., *Priestley*, 1981]. When we refer to the coherence between a scalar quantity, such as wind, and the "the MJO" (a bivariate time series), we mean the multiple coherence between the observed quantity and the two MJO components.

[15] The wind direction over the Gulf of Carpentaria is strongly linked to both the local trade winds and the Australian-Indonesian monsoon. The background flow in this region is dominated by the southeasterly trade winds,

which peak in July. During Austral Summer the Australian-Indonesian monsoon causes the mean flow to be predominantly northwesterly (see *Forbes and Church* [1983] and histogram in Figure 5).
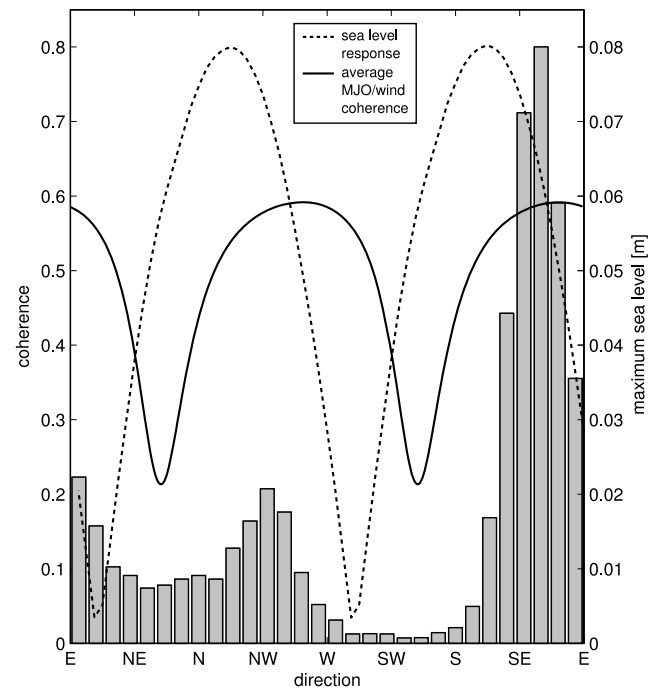
Figure 5. Wind statistics over the Gulf of Carpentaria as a function of wind direction. The shaded boxes form a histogram of daily wind directions of the gulf mean wind. The solid line shows the coherence (averaged over intraseasonal frequencies) between the gulf mean wind, projected onto an axis at the angle given, and the MJO. The dashed line shows the magnitude of the steady state response of gulf mean sea level as a function of wind direction as predicted by the model.
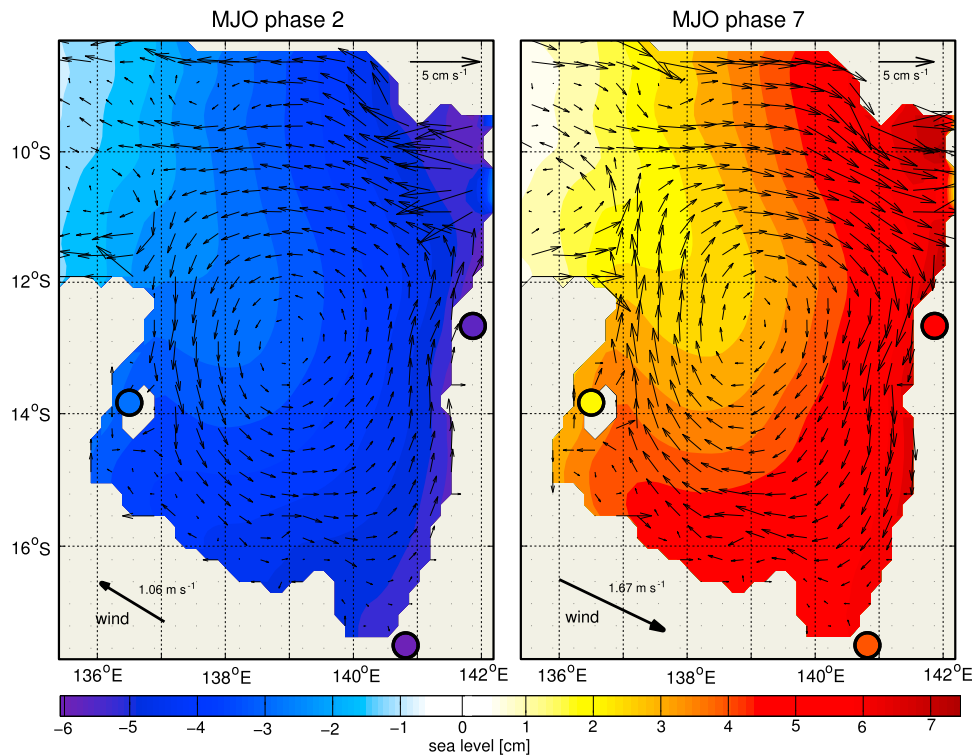

Figure 4. Power spectrum of the MJO and coherence between the MJO and observations of coastal sea level from the Gulf of Carpentaria. Same format as Figure 1.

Figure 6. Composites of sea level, wind, and surface current anomalies associated with (left) phase 2 and (right) phase 7 of the MJO (for MJO amplitudes exceeding 1). The arrows in each bottom left corner are the composites of the gulf-wide wind. The solid contours and solid circles show the composites of η_m and η_o, respectively. The black arrows show composites of predicted currents with reference speed shown at the top right.

[16] To examine the relationship between the MJO index and gulf mean wind we calculated the coherence as a function of frequency (Figure 1). In general, the coherence peaks for both wind components for periods between 30 and 60 days. Zonal wind has the highest coherence with the MJO (between 0.5 and 0.7 across the intraseasonal band). Directional dependence was explored by looking at the average intraseasonal coherence (periods between 30 and 90 days) between the MJO and wind projected onto an axis. The coherence was then plotted as a function of axis direction (Figure 5). The intraseasonal coherence peaks for westerly to northwesterly winds (or easterly to southeasterly). We noted in this section that the prevailing winds in the region are northwesterly/southeasterly. We show in section 5.1 that the gulf responds most strongly to wind in this direction. We therefore anticipate a strong contribution from the MJO to intraseasonal wind-driven variability of sea level and circulation in this region.

[17] Another way of exploring the dependence of wind and sea level on the MJO is by compositing based on its phase. The MJO phases are defined following the work of *Wheeler and Hendon* [2004]: phases 2/3 represent an active MJO over the Indian Ocean, 4/5 over the Maritime Continent, 6/7 over the Western Pacific, and 8/1 over the Western Hemisphere and Africa. Composites of zonal wind show the passage of a convergence region at the surface associated with the movement of active MJO-related convection over the Mar-

itime Continent [e.g., *Zhang*, 2005]. This leads to anomalous easterlies over the Maritime Continent at the equator when the convective center is over the Indian Ocean (phases 1–3) and anomalous westerlies when it is over the Pacific Ocean (phases 6 and 7). The Gulf of Carpentaria, just south of the Maritime Continent, experiences anomalous northwesterlies during phases 6 and 7 with setup of coastal sea level evident at all three tide gauges and anomalous southeasterlies during phases 1–3 with setdown at all three stations (illustrated for phases 2 and 7 in Figure 6).

[18] To explore the seasonal variation of the spectral properties of the wind and the MJO we first calculated spectra using 180 day subsets of the gulf mean wind time series with successive blocks shifted by 1 day. The seasonal cycle of spectral density was then calculated by averaging across years for 1 January, 2 January, etc. The seasonal variation of the northwesterly wind spectrum (Figure 7, left) shows that the energy is relatively high at periods between 30 and 60 days during Austral summer, which coincides with the Australian-Indonesian monsoon. This time of year also corresponds to relatively high coherence between the wind and the MJO (Figure 7, right), consistent with previous work [*Salby and Hendon*, 1994; *Zhang and Dong*, 2004; *Bellenger and Duvel*, 2007]. The seasonal cycle in the spectral density of η_o shows the same cycle as the wind (compare Figure 8, left, with Figure 7, left). In section 5 we
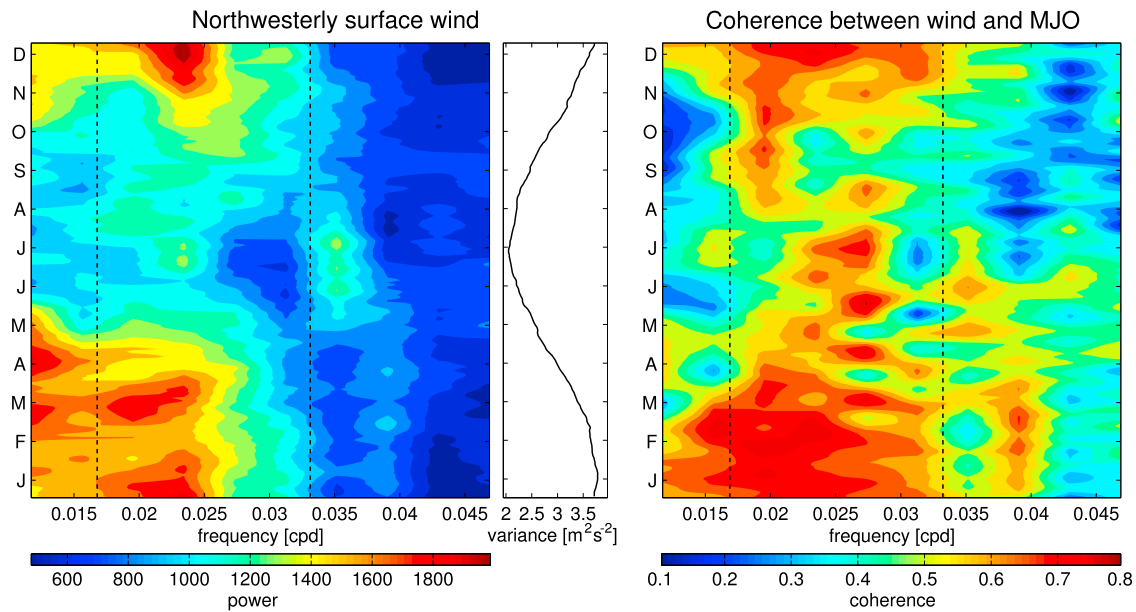
Figure 7. Seasonal variation of the spectral properties of the gulf mean wind. (left) Seasonal cycle of the spectral density of northwesterly wind across the intraseasonal band. (middle) To emphasize the seasonal changes in spectral shape, the spectrum for a given time of year was normalized by the corresponding variance. (right) Seasonal cycle of the coherence between northwesterly wind and the MJO across the intraseasonal band. Vertical lines indicate periods of 30 and 60 days.

check if the ocean model can reproduce these seasonal variations in the spectral properties of sea level.

4. Numerical Model

[19] The Princeton Ocean Model [e.g., *Blumberg and Mellor*, 1987] was used to dynamically simulate the Gulf of Carpentaria, the adjacent shallow Arafura and Timor seas, and the deep waters to the northeast and northwest of Australia (see Figure 3). The model is fully nonlinear and defined on an Arakawa C-grid with a spatial resolution of 1/6° (103 points meridionally and 157 points zonally for a total of 16,171 grid points). The bathymetry (Figure 3) was interpolated to the model grid from the 1/10° Australian Bathymetry and Topography Grid (David Griffin, CSIRO, personal communication). The model is forced by surface stress derived from 6 h reanalysis surface winds linearly interpolated to the model time step (see below). Note that the model is not forced by variations in atmospheric pressure.

[20] The model was run barotropically to simulate sea level and the depth-averaged flow. The bottom stress was formulated in terms of depth averaged flow ($\vec{u}$) and was of the form $c_d\,\vec{u}|\vec{u}|$, where $c_d = 2.5 \times 10^{-3}$. The time step for the barotropic calculations was 12 s. The coastal boundary condition was no normal flow and no slip; radiation conditions were applied at the open boundaries to allow transients generated within the domain to escape with minimal reflection. The initial condition was a state of rest and a flat sea surface. The model was run for 31 years (forced by the reanalysis wind field) and sea level and current fields were

output daily (sufficient for our purposes because our interest is variability on intraseasonal timescales).
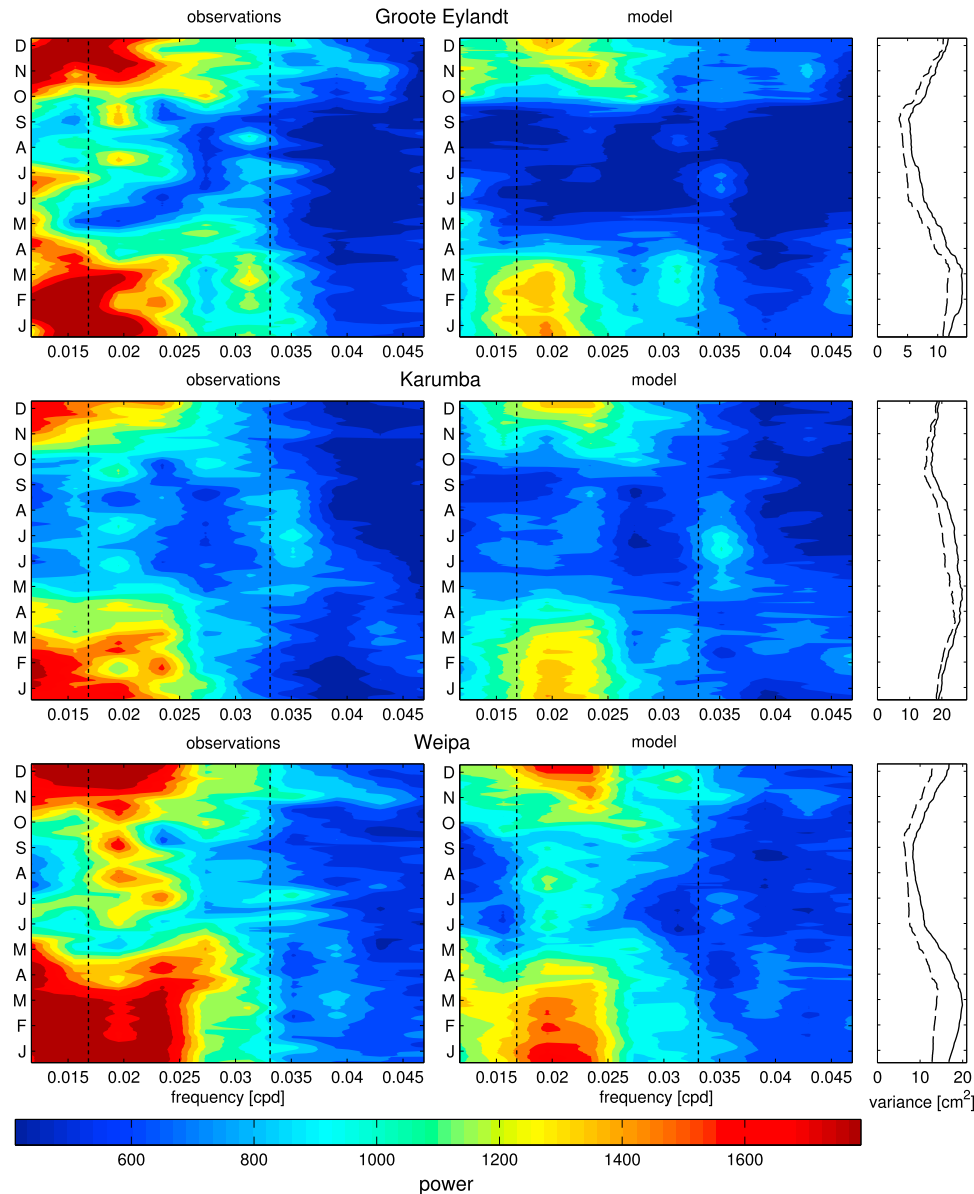
5. Comparison of Observed and Predicted Sea Level

[21] The predicted sea level and circulation in the Gulf of Carpentaria for the period 1 January 1979 to 31 December 2009 was used to explore the forcing mechanisms that link intraseasonal variability in sea level and circulation to the Madden-Julian Oscillation. After evaluating the effect of natural resonances of the model, we compared the model predictions to observations at the three tide gauge locations.

5.1. Dynamical Response of the Gulf to Wind Forcing

[22] To link sea level variability in the gulf with the MJO we must rule out the possibility of a natural resonance with frequencies within the MJO band (such as an internal seiche). To quantify the resonance characteristics of the model, it was forced for 700 days by periodic along-gulf winds (northwesterly direction with an amplitude of 7.1 m s^{-1}). Individual runs were performed for forcing periods between 2 and 150 days. For each run, the amplitude of the gulf mean sea level was calculated and plotted against frequency (not shown). Over intraseasonal timescales the gain is flat, consistent with the work of *Pariwono et al.* [1986], who estimated the resonant period of the Gulf of Carpentaria to be about 26 h. We conclude the model is not resonant at intraseasonal frequencies.

[23] We next examined the sensitivity of sea level to the direction of surface wind. The model was forced for 1 year by a steady, uniform wind of 5 m s^{-1}. Simulations were run

Figure 8. Seasonal variation of the spectral density of observed and predicted sea level: (left) observations, (middle) predictions, and (right) variances by which the spectra have been normalized (solid lines are observations and dashed lines are predictions). Otherwise the format is the same as Figure 7.

independently for 64 discrete wind directions. For each run, the steady state response of the gulf mean sea level was averaged over days 201 through 365 and stored. The largest sea level response was found for northerly to northwesterly winds for setup and the opposite directions for setdown (Figure 5, dashed line), consistent with the discussion in section 3.

5.2. Seasonality in Observed and Predicted Sea Level

[24] Predicted seasonal cycles (estimated by harmonic regression) are of smaller amplitude (10–20 cm) than the observed seasonal cycles. However, our model does not include steric effects which are present in the observations. *Forbes and Church* [1983] calculated the seasonal cycle of steric sea level anomalies to have an amplitude of 9.4 cm at Karumba, which is consistent with our results. The residual seasonal cycle, calculated by subtracting the predicted annual cycle from the observed annual cycle, is similar across all stations. This is consistent with steric changes in the adjacent deep water which peaks near the end of the Southern Hemisphere warming cycle. The model predictions of sea level at the three tide gauge locations were then deseasonalized by removing the annual cycle and its first two harmonics using least squares (henceforth denoted by η_m). After deseasonalization, observed and predicted sea levels agreed quite well in terms of amplitude and correlation (Figure 2 and Table 2). On intraseasonal timescales, the agreement between η_o and η_m is particularly high, with coherence above 0.80 for Groote Eylandt and Weipa, and above 0.7 for Karumba. From Table 2, we can see that the RMS of the prediction errors is generally less than 8 cm (except at Karumba, which are as high as ~12.5 cm).

Table 2. Comparison of Observed and Predicted Sea Level[a]

Name	σ_o	σ_m	σ_{o-m}	ρ_{om}
Groote Eylandt	9.38	8.65	6.24	0.763
Karumba 1	13.18	13.27	12.38	0.562
Karumba 2	15.86	14.13	10.98	0.737
Weipa 1	10.86	9.63	7.45	0.741
Weipa 2	11.70	10.27	6.41	0.837

[a]The standard deviation of η_o and η_m (σ_o and σ_m, respectively), the standard deviation of their difference (σ_{o-m}), and correlation (ρ_{om}) are shown. Note η_o and η_m were high-pass filtered with a cutoff period of half a year prior to the calculation of these statistics. Standard deviations are given in cm.

[25] We were also encouraged to find that the model captures well the observed seasonal cycle of intraseasonal variability (Figure 8, right) except at very low intraseasonal frequencies (<0.015 cpd). Interestingly, the seasonally stratified coherences between η_o and η_m (not shown) are above 0.9 (0.8 for Karumba) during Austral summer but drop to about 0.75 during Austral winter when the connection with the MJO through surface wind forcing is weak. We conclude that the model captures the wind-driven intraseasonal component of sea level variability in the Gulf of Carpentaria.

5.3. Influence of the MJO on Circulation and Sea Level

[26] The composites of model-predicted sea level and depth-averaged current anomalies were calculated as a function of MJO phase. The composites for phases 2 and 7 (Figure 6) illustrate that the wind during this phase is consistent with sea level setup and setdown, respectively. The phase 7 (2) composite of depth-averaged currents exhibits a cyclonic (anticyclonic) gyre centered in the Gulf of Carpentaria and strong eastward (westward) flow through the

Torres Strait. As the MJO performs a cycle, the composites pass through a quiescent state (phase 8), followed by the setdown pattern (phase 1–3), and then another quiescent state (phases 4 and 5), before returning to the setup pattern (phases 6 and 7).

[27] We can generate a time series that represents setup and setdown favorable conditions by projecting the bivariate MJO index onto the phase 3–phase 7 axis. By definition, positive values occur during phase 7 and negative values during phase 3. From Figure 9 we can see that strong setup and setdown events often occur when the MJO is of extreme amplitude during phases 7 and 3, respectively. It is also clear from Figure 9 that this connection is particularly strong during Austral summer.

[28] The predicted sea level does not reproduce well the observed variability on timescales longer than 120 days (Figure 2). The physical origin of this low-frequency signal is discussed in section 6.

## 6. Cause of Low-Frequency Residual Variability

[29] By removing the model predictions from the observed coastal sea level, we are left with a residual, η_{o-m}, unexplained by the dynamical model. Removing η_m from η_o effectively removes the high-frequency local wind effect, leaving a low-frequency residual that is very similar at each tide gauge location (correlations above 0.7). To obtain a single regional signal, we averaged the three η_{o-m} series into one (henceforth denoted by $\overline{\eta}_{o-m}$). The variations of $\overline{\eta}_{o-m}$ are on the order of 10–20 cm (Figure 10, top).

[30] What is the cause of variability of $\overline{\eta}_{o-m}$? It is not present in the surface wind forcing and so it is likely due to variations in the deeper waters along the open boundaries of the model domain. Figure 10 compares $\overline{\eta}_{o-m}$ and altimeter-observed sea level from a point at the shelf edge (denoted by
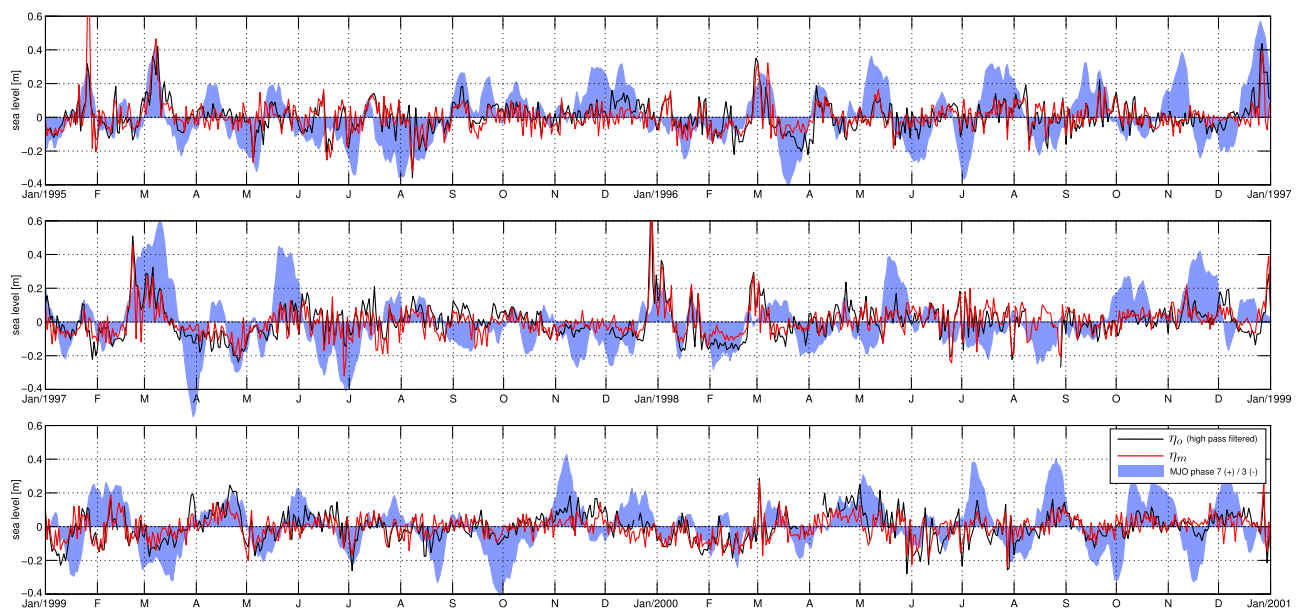
Figure 9. Observed and predicted sea level at Groote Eylandt over a typical 6 year period. Black line is η_o after high-pass filtering with a cutoff period of half a year, red line is η_m, and blue shading is the MJO index, projected onto the phase 7–phase 3 axis (positive values correspond to phase 7 and negative values to phase 3).
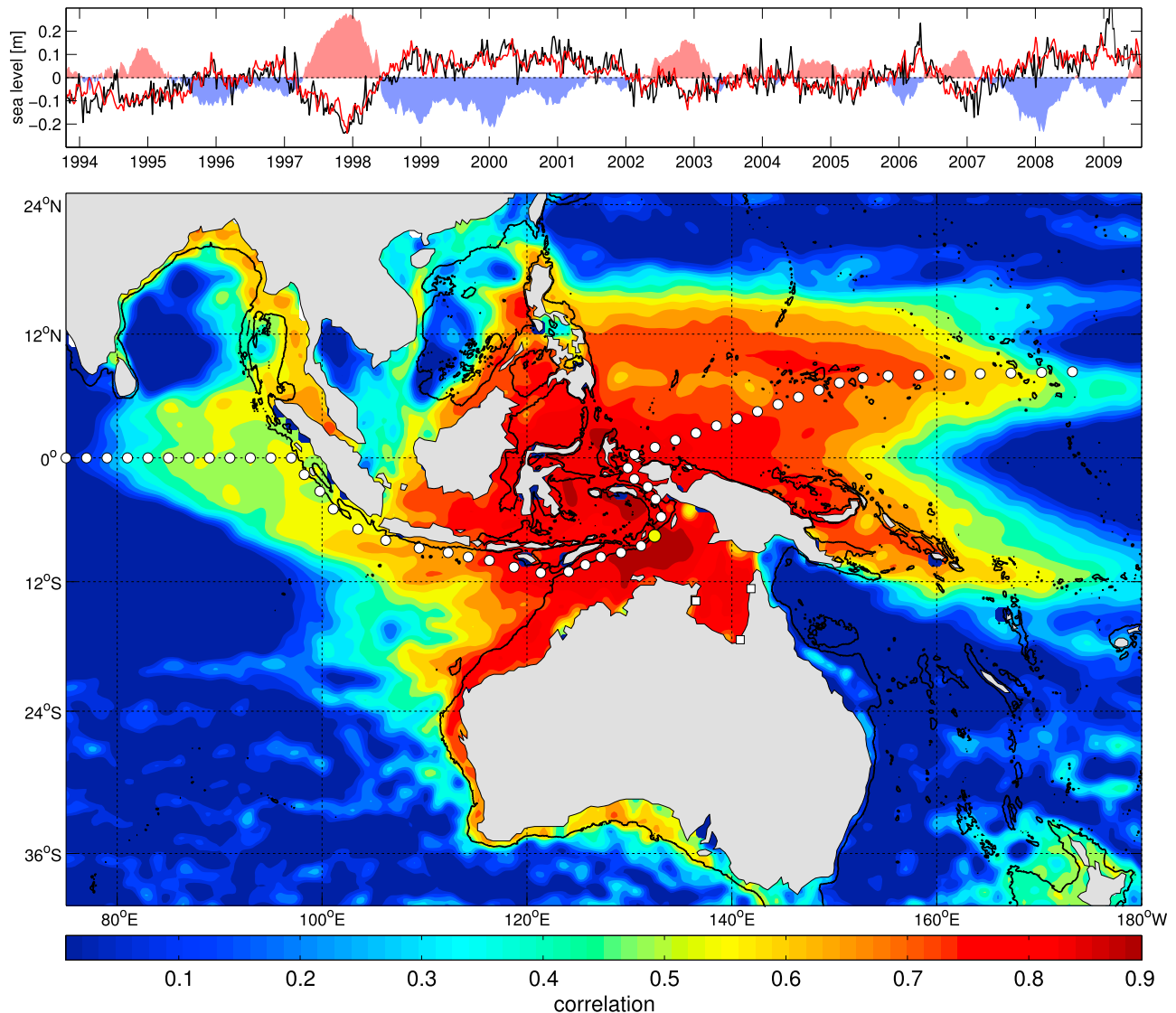
Figure 10. Time series and correlations of low-frequency sea level. (top) The $\overline{\eta}_{o\text{-}m}$ is shown in black and η_{sh}, sea level from (132.45°E, 7.60°S) (yellow circle, Figure 10, bottom), is shown in red. The Niño 3.4 index, I_{EN}, is shown by the blue and red shading. (bottom) Correlation between altimeter-measured sea level, low-pass filtered with a cutoff period of half a year, and $\overline{\eta}_{o\text{-}m}$. The black line is the 1000 m depth contour. Open circles are positions from which altimeter records were extracted for the Hovmöller diagrams in Figure 12.

η_{sh}; see caption for exact location). The close agreement between $\overline{\eta}_{o\text{-}m}$ and η_{sh} leads us to hypothesize that the unexplained low-frequency variability is driven by larger-scale sea level changes in the deeper water, seaward of the Gulf of Carpentaria.

[31] What is the cause of the variability of η_{sh}? Equatorial Kelvin waves can be excited by surface winds blowing over the Indian Ocean, which then propagate eastward across the basin. Once they reach the eastern boundary they can be channeled toward the Indonesian Throughflow region as coastal trapped waves along the western coast of the Indonesian Archipelago. Similarly, westward propagating Rossby waves from the tropical Pacific can enter the throughflow region upon reaching the western ocean boundary [*Spall and*

Pedlosky, 2005]. This raises the question of which ocean basin is the primary source of the variability of η_{sh}. *Clarke and Liu* [1994] predicted that signals originating in the Indian Ocean would travel no further than the Lombok Strait. They also predicted, and showed with sea level observations along the northwestern Australian coast, that Pacific Ocean signals can penetrate the Indonesian Throughflow region and propagate along the western Australian coast. It is therefore not surprising that interannual sea level changes along the western boundaries of the Indonesian Archipelago and western Australia are in phase and highly correlated with sea level in the western Pacific [*Clarke*, 1991]. More recent studies have supported the view that a significant part of the variability of Australian coastal sea level originates in the

Pacific Ocean [*Pariwono et al.*, 1986; *Potemra*, 2001; *Wijffels and Meyers*, 2004]. It has been shown that a positive ENSO phase is associated with a drop in sea level in the waters surrounding Indonesia [*Nerem et al.*, 1999]. This drop is consistent with a quasi-steady response to low-frequency wind forcing in the Pacific which is in turn related to ENSO [*Clarke*, 2008]. We have used three approaches to explore the origin of the low-frequency variability in the Gulf of Carpentaria as detailed in sections 6.1–6.3.

6.1. Correlations of Sea Level with Climatalogical Indices

[32] The Niño 3.4 index, I_{EN}, was used as a measure of Pacific Ocean variability and the dipole mode index [*Saji et al.*, 1999], I_{DMI}, was used as a measure of Indian Ocean variability. (Both were obtained from http://ioc-goos-oopc.org/state_of_the_ocean/all/-goos-oopc.org/state_of_the_ocean/all/.) For periods longer than 1 year, $\overline{\eta}_{o\text{-}m}$ is coherent with I_{EN} and I_{DMI} at about 0.8 and 0.4, respectively (both significant at the 5% level). This could lead one to conclude that both oceans contribute significantly to the variability of $\overline{\eta}_{o\text{-}m}$. However, these two indices are not independent [*Saji and Yamagata*, 2003; *Yuan and Li*, 2008], and we used partial coherence to remove the effect of one index on the coherence between $\overline{\eta}_{o\text{-}m}$ and the other index [*Priestley*, 1981]. The partial coherence between the $\overline{\eta}_{o\text{-}m}$ and I_{EN}, allowing for I_{DMI}, is about 0.7 for periods exceeding 1 year (see Figure 10 for time series); the corresponding partial coherence between $\overline{\eta}_{o\text{-}m}$ and I_{DMI}, allowing for the effect of I_{EN}, is not significant at the 5% level. This simple analysis leads us to speculate that $\overline{\eta}_{o\text{-}m}$ is forced primarily by large-scale, ENSO-related variability in the Pacific Ocean rather than in the Indian Ocean.

6.2. Regional Sea Level Correlations

[33] Correlations between $\overline{\eta}_{o\text{-}m}$ and sea level from altimeters were calculated on a 1/4° grid and contoured (Figure 10). The patterns formed by the high correlations (above 0.4) suggest connections between the Indian and Pacific Oceans and the Gulf of Carpentaria. In the Indian Ocean there is a tongue of high correlation extending from the eastern equatorial boundary which encompasses Sumatra as well as extending poleward both north, around the Bay of Bengal, and south, along the Indonsian Archipelago. In the Pacific Ocean there are two extended tongues of high correlation in the tropics, north and south of the equator. Finally, there is a long narrow tongue hugging the coast of Australia that links Tasmania back to the Indian and Pacific oceans.

[34] To identify the source regions for the variability in the Gulf of Carpentaria, we mapped the correlation between sea level on the 1/4° grid with sea level at various potential source locations. By examining the associated time lags (not shown) in the high-correlation regions, we conclude that there are in fact only two potential sources for the variability: the equatorial Indian Ocean and the northern tongue of high correlation in the tropical Pacific Ocean (see Figures 11a and 11b). Noting the high correlation in the gulf, one might conclude that both oceans are important drivers of variability in this region. However, as noted earlier, variability in the Indian and Pacific oceans are not independent and so partial correlations were calculated as before to quantify the effect

of each basin separately (see Figures 11c and 11d). The maps of partial correlation clearly show that the variability originating in the Indian Ocean does not propagate past the Lombok Strait, consistent with the work of *Clarke and Liu* [1994]. On the other hand, variability from the Pacific Ocean can reach the Gulf of Carpentaria and can continue to propagate west and south around the coast of Australia.

[35] The partial correlation map for the Pacific Ocean source region (and the corresponding lag map, not shown) are consistent with equatorial Rossby waves propagating westward across the basin and entering the Indonesian Throughflow region. The partial correlation and lag maps for the Indian Ocean source region are consistent with equatorially trapped Kelvin waves traveling eastward and then poleward as coastally trapped waves toward the Indonesian Throughflow region. These interpretations are consistent with the discussion and references given above.

6.3. Hovmöller Diagrams

[36] To better understand how the two ocean basins influence low-frequency sea level in the Gulf of Carpentaria, we have generated Hovmöller diagrams along the two pathways identified in the previous section. (The advantage of Hovmöller diagrams is that they allow us to identify individual events as well as explicitly show lags as these events propagate.) Both pathways originate in the interior of their respective oceans and terminate at the location of η_{sh} on the northwestern Australian shelf edge. Other potential pathways through the Indonesian Throughflow (such as the channel between Borneo and Sulawesi and exiting through the Lombok strait) were identified but were not explored further in this study. Time series of sea level from the positions shown by white circles in Figure 10 were low-pass filtered with a cutoff period of half a year prior to plotting. The time axis of the Hovmöller diagram runs from 1994 to 2009.

[37] The Hovmöller diagram for the Indian Ocean (Figure 12, left) shows that signals from the equatorial Indian Ocean are channeled along the coast of Indonesia but are severely attenuated when crossing the Lombok Strait as predicted by *Clarke and Liu* [1994]. Signals traveling along the equator propagate at the expected speed of equatorial Kelvin waves (2.8 m s^{-1} [*Chelton et al.*, 1998]); the speed of propagation along the Indonesian coast agrees well with previous estimates (1.78 m s^{-1} for coastal South America [*Spillane et al.*, 1987; see also *Arief and Murray*, 1996]).

[38] The Hovmöller diagram for the Pacific Ocean (Figure 12, right) shows that signals originating in this basin propagate westward and then through the Indonesian Archipelago and along the Australian shelf break, where they force sea level in the shallow Timor and Arafura seas and the Gulf of Carpentaria. In fact, we can often see evidence of these signals propogating past the location of η_{sh} and continuing along the Australian shelf edge (i.e., large event in 1994–1995). These westward propagating signals travel at wave speeds which match well with the first- and second-mode equatorial Rossby wave speeds (0.93 and 0.47 m s^{-1}, respectively [*Chelton et al.*, 2003]).

[39] Overall the correlations with indices, regional sea level correlations, and Hovmöller diagrams are consistent with our conclusion that the low-frequency variability in the
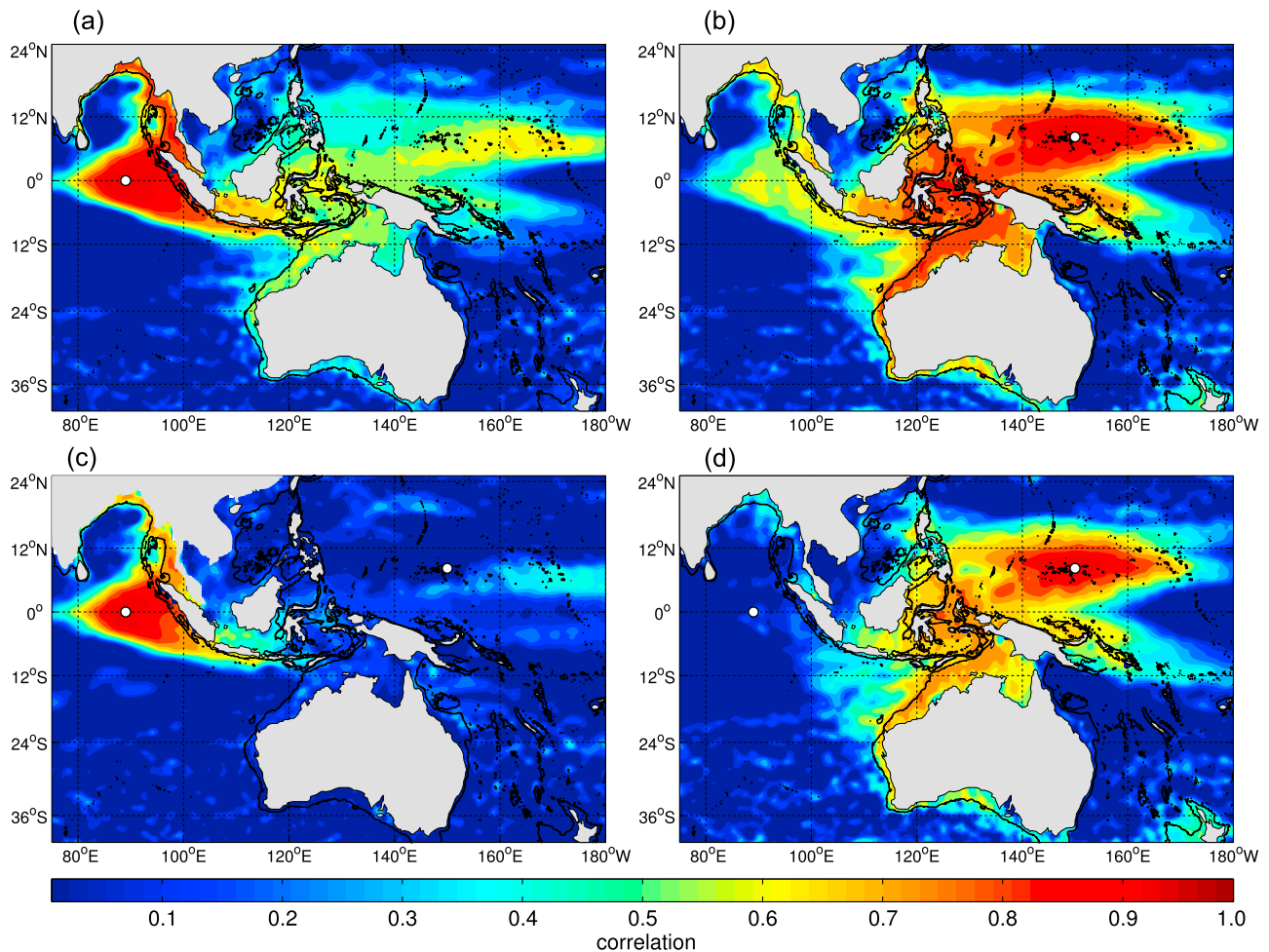
Figure 11. Connections between the Indian and Pacific oceans and the Gulf of Carpentaria. Correlation between gridded altimeter sea levels and sea level at (a) (0°N, 89°E) in the Indian Ocean source region and (b) (8.25°N, 150°E) in the Pacific Ocean source region. (c and d) Partial correlations allowing for the effect of the other source region. Locations of sources are indicated by white dots. The thin black lines are the 1000 m depth contour.

Gulf of Carpentaria is dominated by energy originating in the Pacific Ocean rather than the Indian Ocean.

7. Summary and Discussion

[40] We have used a barotropic circulation model to show that sea level variability in the shallow waters of the Gulf of Carpentaria is dominated by simple wind setup. The same model was also used to map out the associated depth-averaged flow and thus supplement and extend the study of OT10 that used simple dynamical balances to demonstrate the importance of setup in this region.

[41] A reconstruction of sea level and circulation variability driven by observed winds for the period 1979–2009 showed that the model could reproduce many of the features present in three long-observed sea level records from the gulf. The timing and amplitude of the seasonal cycles were consistent with the observations once the effects of density were taken into account. After deseasonalization, the amplitudes of the predictions were similar to that of the observations; correlations between observed and predicted

sea level at tide gauge locations were typically above 0.8 on intraseasonal timescales. Furthermore, the predictions capture the seasonal cycle of the spectral properties of the observations.

[42] The along-gulf wind is strongly correlated with the Madden-Julian Oscillation. As the center of convection propagates from the Indian Ocean to the Pacific Ocean, low-level wind anomalies dominate the wind variability over the gulf. Thus, changes in sea level and circulation in the gulf are associated with a larger-scale atmospheric mode of intraseasonal variability. This has implications for predictability of sea level and circulation in the gulf; if we can reliably predict the initiation and evolution of the MJO, which can be done out to 15 days empirically [*Lo and Hendon*, 2000; *Maharaj and Wheeler*, 2005; *Jiang et al.*, 2008] and 10–20 days dynamically [*Zhang*, 2005; *Lin et al.*, 2008], then this information will lead to better forecast skill for sea level and circulation variability in the Gulf of Carpentaria on intraseasonal timescales.

[43] Subtracting the predictions of sea level from the coastal observations leaves a large-scale low-frequency
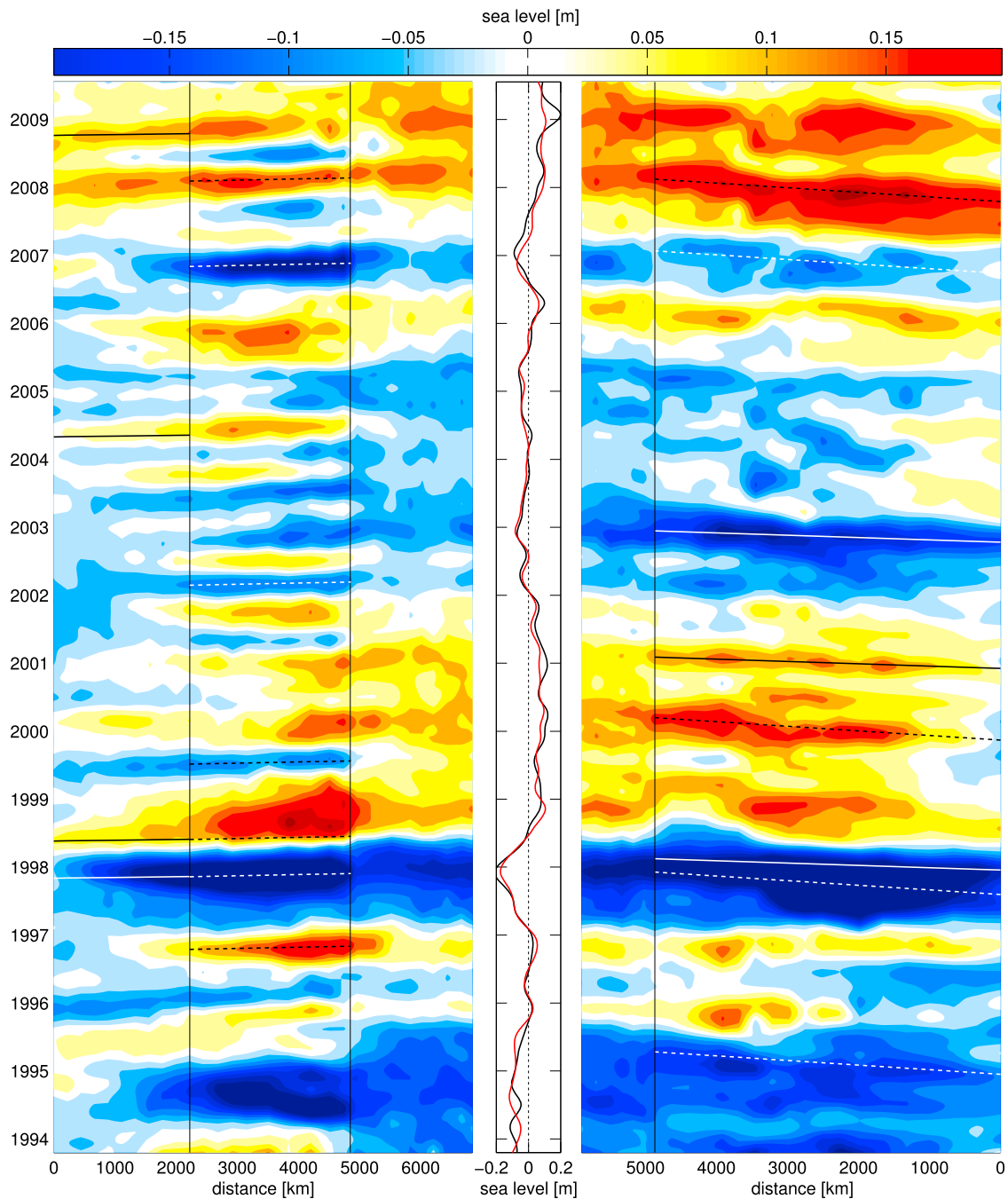
Figure 12. Propagation of signals along pathways originating in the Indian Ocean and the Pacific Ocean and terminating at the location of η_{sh}. (left) Hovmöller diagram for the Indian Ocean pathway. The vertical line at a distance of ~2000 km indicates where the equator meets Sumatra; the second line approximates the location of the Lombok Strait. Sloped lines show equatorial Kelvin wave speeds (2.8 m s^{-1}, solid line) and coastal trapped wave speeds (1.78 m s^{-1}, dashed line). (right) Similar format as Figure 12 (left) but for the Pacific Ocean pathway. The vertical line marks the entrance to the Indonesian Archipelago. Sloped lines show the speeds of first- and second-mode equatorial Rossby waves (0.93 and 0.47 m s^{-1}, respectively). (middle) The $\overline{\eta}_{o-m}$ (black) and η_{sh} (red), low-pass filtered with a cutoff period of half a year. Note that the innermost time series in each Hovmöller diagram also corresponds to η_{sh}.

signal unexplained by the model. The weak spatial gradients and long timescale of this residual mode of variability imply that it will not be associated with significant changes in circulation. To identify the cause of this residual low-frequency signal, we used three statistical approaches. First,

we showed that the large-scale signal was correlated with two indices describing Indian Ocean dipole variability and ENSO variability. However, a more detailed analysis based on partial coherence and correlation suggested the signal

was driven by mainly ENSO-related signals originating in the Pacific Ocean.

[44] The second approach involved calculating correlations among coastal sea level and gridded sea level measurements from altimeters. We were able to identify several possible pathways based on high correlations between the coastal and altimeter observations. By examining lagged correlations we were able to identify two possible source regions for the variability in the gulf: the Indian Ocean and the Pacific Ocean. Again, using partial correlations we were able to show that sea level variations originating in the Pacific pass through the Indonesian Archipelago, unlike those originating in the Indian Ocean. We thus attribute the correlations between sea level in the gulf and Indian Ocean as noncausal (i.e., due to correlations between the forcings of the two ocean basins such as wind stress).

[45] Finally, we constructed Hovmöller diagrams aligned with the pathways connecting the Indian Ocean, the seaward edge of the Gulf of Carpentaria, and the Pacific Ocean. These diagrams confirm the Pacific is the origin of low-frequency sea level variability along the northwestern Australian shelf edge and thus the Gulf of Carpentaria. They also confirm that the Lombok Strait is a barrier to the propagation of signals from the Indian Ocean. We also showed that the low-frequency signal in the gulf is strongly correlated with El Niño. Knowledge of the future state of El Niño, which can be predicted with 6–24 months lead time [*Chen et al.*, 2004; *Jin et al.*, 2008], can therefore be used to predict potential large-scale changes in the gulf on long timescales.

[46] This study confirms that sea level measured by coastal tide gauges can be useful in mapping out large-scale sea level changes in deep water if the effect of local wind is removed. It is likely that the low-frequency changes in sea level in the gulf are also associated with changes in the vertical structure of temperature and salinity (i.e., steric changes), tilts of sea level, and thus changes in surface circulation of the adjacent deep ocean. The inversion of coastal sea level observations to infer such changes in the deep ocean is a difficult problem that will require the use of a fully baroclinic, possibly data-assimilative, ocean circulation model of the region. This study is under way.

References

Arief, D., and S. Murray (1996), Low-frequency fluctuations in the Indonesian throughflow through Lombok Strait, *J. Geophys. Res.*, *101*(C5), 12,455–12,464.

Bellenger, H., and J. Duvel (2007), Intraseasonal convective perturbations related to the seasonal march of the Indo-Pacific monsoons, *J. Clim.*, *20*(12), 2853–2863.

Blumberg, A., and G. Mellor (1987), A description of a three-dimensional coastal ocean circulation model, in *Three-Dimensional Coastal Ocean Models*, *Coastal Estuarine Sci. Ser.*, vol. 4, edited by N. S. Heaps, pp. 1–16, AGU, Washington, D. C.

Bond, N., and G. Vecchi (2003), The influence of the Madden-Julian Oscillation on precipitation in Oregon and Washington, *Weather Forecasting*, *18*(4), 600–613.

Cassou, C. (2008), Intraseasonal interaction between the Madden-Julian Oscillation and the North Atlantic Oscillation, *Nature*, *455*(7212), 523–527.

Chelton, D., R. deSzoeke, M. Schlax, K. El Naggar, and N. Siwertz (1998), Geographical variability of the first baroclinic Rossby radius of deformation, *J. Phys. Oceanogr.*, *28*(3), 433–460.

Chelton, D., M. Schlax, J. Lyman, and G. Johnson (2003), Equatorially trapped Rossby waves in the presence of meridionally sheared baroclinic flow in the Pacific Ocean, *Prog. Oceanogr.*, *56*(2), 323–380.

Chen, D., M. Cane, A. Kaplan, S. Zebiak, and D. Huang (2004), Predictability of El Niño over the past 148 years, *Nature*, *428*(6984), 733–736.

Clarke, A. (1991), On the reflection and transmission of low-frequency energy at the irregular western Pacific Ocean boundary, *J. Geophys. Res.*, *96*(XX), suppl., 3289–3305.

Clarke, A. (2008), *An Introduction to the Dynamics of El Niño and the Southern Oscillation*, Academic, London.

Clarke, A., and X. Liu (1994), Interannual sea level in the northern and eastern Indian Ocean, *J. Phys. Oceanogr.*, *24*(6), 1224–1235.

Doodson, A. (1928), The analysis of tidal observations, *Philos. Trans. R. Soc. London A*, *227*, 223–279.

Enfield, D. (1987), The intraseasonal oscillation in eastern Pacific sea levels: How is it forced?, *J. Phys. Oceanogr.*, *17*(11), 1860–1876.

Forbes, A., and J. Church (1983), Circulation in the Gulf of Carpentaria. Part II. Residual currents and mean sea level, *Aust. J. Mar. Freshwater Res.*, *34*, 11–22.

Fu, L. (2003), Wind-forced intraseasonal sea level variability of the extra-tropical oceans, *J. Phys. Oceanogr.*, *33*(2), 436–449.

Hall, J., A. Matthews, and D. Karoly (2001), The modulation of tropical cyclone activity in the Australian region by the Madden-Julian Oscillation, *Mon. Weather Rev.*, *129*(12), 2970–2982.

Jiang, X., D. Waliser, M. Wheeler, C. Jones, M. Lee, and S. Schubert (2008), Assessing the skill of an all-season statistical forecast model for the Madden-Julian Oscillation, *Mon. Weather Rev.*, *136*(6), 1940–1956.

Jin, E., et al. (2008), Current status of ENSO prediction skill in coupled ocean-atmosphere models, *Clim. Dyn.*, *31*(6), 647–664.

Kalnay, E., et al. (1996), The NCEP/NCAR 40-year reanalysis project, *Bull. Am. Meteorol. Soc.*, *77*(3), 437–471.

Kanamitsu, M., W. Ebisuzaki, J. Woollen, S. Yang, J. Hnilo, M. Fiorino, and G. Potter (2002), NCEP-DOE AMIP-II reanalysis (R-2), *Bull. Am. Meteorol. Soc.*, *83*(11), 1631–1643.

Large, W., and S. Pond (1981), Open ocean momentum flux measurements in moderate to strong winds, *J. Phys. Oceanogr.*, *11*(3), 324–336.

Liebmann, B., H. Hendon, and J. Glick (1994), The relationship between tropical cyclones of the western Pacific and Indian oceans and the Madden-Julian Oscillation, *J. Meteorol. Soc. Jpn.*, *72*(41), 1–412.

Lin, H., and G. Brunet (2009), The influence of the Madden-Julian Oscillation on Canadian wintertime surface air temperature, *Mon. Weather Rev.*, *137*(7), 2250–2262.

Lin, H., G. Brunet, and J. Derome (2008), Forecast skill of the Madden-Julian Oscillation in two Canadian atmospheric models, *Mon. Weather Rev.*, *136*(11), 4130–4149.

Lin, H., G. Brunet, and J. Derome (2009), An observed connection between the North Atlantic Oscillation and the Madden-Julian Oscillation, *J. Clim.*, *22*(2), 364–380.

Lo, F., and H. Hendon (2000), Empirical extended-range prediction of the Madden-Julian Oscillation, *Mon. Weather Rev.*, *128*(7), 2528–2543.

Madden, R., and P. Julian (1971), Detection of a 40–50 day oscillation in the zonal wind in the tropical Pacific, *J. Atmos. Sci.*, *28*(5), 702–708.

Madden, R., and P. Julian (1972), Description of global-scale circulation cells in the tropics with a 40–50 day period, *J. Atmos. Sci.*, *29*(6), 1109–1123.

Maharaj, E., and M. Wheeler (2005), Forecasting an index of the Madden-Oscillation, *Int. J. Climatol.*, *25*(12), 1611–1618.

Maloney, E., and D. Hartmann (2000a), Modulation of eastern North Pacific hurricanes by the Madden-Julian Oscillation, *J. Clim.*, *13*(9), 1451–1460.

Maloney, E., and D. Hartmann (2000b), Modulation of hurricane activity in the Gulf of Mexico by the Madden-Julian Oscillation, *Science*, *287*(5460), 2002–2004.

Maloney, E., D. Chelton, and S. Esbensen (2008), Subseasonal SST variability in the tropical eastern North Pacific during boreal summer, *J. Clim.*, *21*(17), 4149–6167.

McBride, J., and W. Frank (1999), Relationships between stability and monsoon convection, *J. Atmos. Sci.*, *56*(1), 24–36.

Nerem, R., D. Chambers, E. Leuliette, G. Mitchum, and B. Giese (1999), Variations in global mean sea level associated with the 1997–1998 ENSO event: Implications for measuring long term sea level change, *Geophys. Res. Lett.*, *26*(19), 3005–3008.

Oliver, E., and K. Thompson (2010), Madden-Julian Oscillation and sea level: Local and remote forcing, *J. Geophys. Res.*, *115*, C01003, doi:10.1029/2009JC005337.

Pariwono, J., J. Bye, and G. Lennon (1986), Long-period variations of sea-level in Australasia, *Geophys. J. R. Astron. Soc.*, *87*(1), 43–54.

Pawlowicz, R., B. Beardsley, and S. Lentz (2002), Classical tidal harmonic analysis including error estimates in MATLAB using T_TIDE, *Comput. Geosci.*, *28*(8), 929–937.

Pearce, A., and B. Phillips (1988), ENSO events, the Leeuwin Current, and larval recruitment of the western rock lobster, *ICES J. Mar. Sci.*, *45*(1), 13–21.

Potemra, J. (2001), Contribution of equatorial Pacific winds to southern tropical Indian Ocean Rossby waves, *J. Geophys. Res.*, *106*(C2), 2407–2422.

Priestley, M. (1981), *Spectral Analysis and Time Series*, Academic, New York.

Saji, N., and T. Yamagata (2003), Possible impacts of Indian Ocean dipole mode events on global climate, *Clim. Res.*, *25*(2), 151–169.

Saji, N., B. Goswami, P. Vinayachandran, and T. Yamagata (1999), A dipole mode in the tropical Indian Ocean, *Nature*, *401*(6751), 360–363.

Salby, M., and H. Hendon (1994), Intraseasonal behavior of clouds, temperature, and motion in the tropics, *J. Atmos. Sci.*, *51*(15), 2207–2224.

Shinoda, T., H. Hendon, and J. Glick (1998), Intraseasonal variability of surface fluxes and sea surface temperature in the tropical western Pacific and Indian oceans, *J. Clim.*, *11*(7), 1685–1702.

Spall, M., and J. Pedlosky (2005), Reflection and transmission of equatorial Rossby waves, *J. Phys. Oceanogr.*, *35*(3), 363–373.

Spillane, M., D. Enfield, and J. Allen (1987), Intraseasonal oscillations in sea level along the west coast of the Americas, *J. Phys. Oceanogr.*, *17*(3), 313–325.

Tregoning, P., K. Lambeck, and G. Ramillien (2008), GRACE estimates of sea surface height anomalies in the Gulf of Carpentaria, Australia, *Earth Planet. Sci. Lett.*, *271*(1–4), 241–244.

Vance, D., D. Staples, and J. Kerr (1985), Factors affecting year-to-year variation in the catch of banana prawns (*Penaeus merguiensis*) in the Gulf of Carpentaria, Australia, *ICES J. Mar. Sci.*, *42*(1), 83–97.

Vecchi, G., and N. Bond (2004), The Madden-Julian Oscillation (MJO) and northern high latitude wintertime surface air temperatures, *Geophys. Res. Lett.*, *31*, L04104, doi:10.1029/2003GL018645.

Vialard, J., S. Shenoi, J. McCreary, D. Shankar, F. Durand, V. Fernando, and S. Shetye (2009), Intraseasonal response of the northern Indian Ocean coastal waveguide to the Madden-Julian Oscillation, *Geophys. Res. Lett.*, *36*, L14606, doi:10.1029/2009GL038450.

Webber, B., A. Matthews, and K. Heywood (2010), A dynamical ocean feedback mechanism for the Madden-Julian Oscillation, *Q. J. R. Meteorol. Soc.*, *136*(648), 740–754.

Wheeler, M., and H. Hendon (2004), An all-season real-time multivariate MJO index: Development of an index for monitoring and prediction, *Mon. Weather Rev.*, *132*(8), 1917–1932.

Wijffels, S., and G. Meyers (2004), An intersection of oceanic waveguides: Variability in the Indonesian throughflow region, *J. Phys. Oceanogr.*, *34*(5), 1232–1253.

Yuan, Y., and C. Li (2008), Decadal variability of the IOD-ENSO relationship, *Chin. Sci. Bull.*, *53*(11), 1745–1752.

Zhang, C. (2005), Madden-Julian Oscillation, *Rev. Geophys.*, *43*, RG2003, doi:10.1029/2004RG000158.

Zhang, C., and M. Dong (2004), Seasonality in the Madden-Julian Oscillation, *J. Clim.*, *17*(16), 3169–3180.

Zhang, X., Y. Lu, and K. Thompson (2009), Sea level variations in the tropical Pacific Ocean and the Madden-Julian Oscillation, *J. Phys. Oceanogr.*, *39*(8), 1984–1992.

E. C. J. Oliver and K. R. Thompson, Department of Oceanography, Dalhousie University, 1355 Oxford St., Halifax, NS B3H 4J1, Canada. (eric.oliver@dal.ca; keith.thompson@dal.ca)